This article has been accepted for publication in a future issue of this journal, but has not been fully edited. Content may change prior to final publication. Citation information: DOI 10.1109/TAP.2015.2449894, IEEE Transactions on Antennas and Propagation

Topology Optimization of Planar Antennas for Wideband Near-Field Coupling

Emadeldeen Hassan, Daniel Noreland, Robin Augustine, Eddie Wadbro, and Martin Berggren

***Abstract*—We present an approach to design from scratch planar microwave antennas for the purpose of ultra-wideband near-field sensing. Up to about 120,000 design variables associated with square grids on planar substrates are subject to design, and a numerical optimization algorithm decides, after around 200 iterations, for each edge in the grid whether it should consist of metal or a dielectric. The antenna layouts produced with this approach show ultra-wideband impedance matching properties and near-field coupling coefficients that are flat over a much wider frequency range than a standard ultra-wideband antenna. The properties of the optimized antennas are successfully cross-verified with a commercial software and, for one of the designs, also validated experimentally. We demonstrate that an antenna optimized in this way shows a high sensitivity when used for near-field detection of a phantom with dielectric properties representative of muscle tissue.**

***Index Terms*—adjoint-field problem, ultra-wideband antennas (UWB), directivity, Vivaldi antenna, microwave sensing.**

I. Introduction

For decades, there have been efforts to design and develop various types of wideband antennas, for instance planar monopole, bow-tie, and spiral antennas [1]–[3]. Generally, the main concern has been to achieve wide impedance bandwidth and a stable omni-directional radiation pattern. However, the use of omni-directional antennas for sensing purposes might cause either interference with unwanted environmental objects or a waste of parts of the radiated energy in unwanted directions. It may therefore be beneficial to employ wideband directive antennas to achieve robust detection and sensing systems.

A class of antennas that can achieve both wideband and directional operation is the travelling wave antennas [3, ch 10]. An example is the tapered slot antenna, known as the Vivaldi antenna, or its variant the antipodal Vivaldi antenna [4], [5]. There have been many efforts to tailor the performance of the Vivaldi antennas in terms of their operational bandwidth or directivity. However, a conventional Vivaldi antenna is generally described by few parameters, which limits the possibility to find adequate solutions. A focus on enlarging the impedance bandwidth of Vivaldi antennas might reduce the required directivity, especially at the lower frequencies where the antenna arms can radiate as monopoles. It is therefore essential to account for both the antenna directivity and the impedance bandwidth to obtain an overall favorable performance. Bourqui *et al.* [6] proposed an improvement of the near-field directivity of an antipodal Vivaldi antenna by introducing a dielectric director in the tapered slot. However, the director was mainly effective for the higher frequencies.

A different approach to obtain wideband directive antennas is to use artificial magnetic conductors (AMC) as reflectors. However, there still exist challenges to design such wideband AMC [7]. Yang and Kishk [8] introduced the self-grounded bow-tie antenna as a low-profile wideband directive antenna. However, their antenna requires a separate feeding network to be matched with conventional 50 Ohm feed lines.

One approach to the design of antennas with particular properties is to formulate the design problem as an optimization problem. Recently, we proposed an approach to design complex antenna structures in a computationally efficient way by using the material distribution approach to topology optimization [9]. We introduced various antenna designs, such as ultra-wideband monopole antennas and patch antennas operating at multi-frequency bands [9]. In addition, we presented designs for the whole antenna structure including the antenna ground plane [10].

In this work, we use the same approach to introduce new wideband directive antennas that can be used to improve the sensitivity of microwave detection and imaging systems. To design such antennas, we formulate an optimization problem with the objective to maximize the coupling coefficient, $|S_{21}|$, between two antennas separated by a specific distance and at the same time to minimize the antenna reflection coefficient $|S_{11}|$. We validate the performance of our designs by measurements and also cross-verify the simulations with the CST Microwave Studio package (https://www.cst.com/). In addition, we include simulation and measurement studies illustrating the sensing capabilities of the optimized antennas when used to detect a phantom that simulates human muscle tissues. We emphasize that the main goal is to optimize the *near-field* coupling and to investigate the performance in the near-field.

II. Material distribution topology optimization

The material distribution approach to topology optimization, originally developed for the design of load-bearing elastic structures [11], has been used to design various electromagnetic devices [9], [12]–[16]. In this approach, a density function is used to express the distribution of a material in a given domain. Typically, the density function is sampled into a density vector $\boldsymbol{p} = [p_1, p_2, \cdots, p_M]$. Each component p_i of the the density vector is assigned to an element i in the design domain to indicate presence, $p_i = 1$, or absence, $p_i = 0$, of a material. During the optimization of a particular objective function, the components of the density vector are allowed to take values between 0 and 1, but by the end of the process, the vector $\boldsymbol{p}$ must hold binary values only.

III. Problem Formulation

Fig. 1 illustrates the problem setup. Two antennas, Antenna 1 and Antenna 2, whose topologies we aim to optimize, are located in the design domains Ω^1 and Ω^2, respectively. Two 50 Ohm coaxial cables, separated by a distance d_f, are connected through a ground plane Γ_0 to Ω^1 and Ω^2,

Manuscript received December 16, 2014. The authors are with the Department of Computing Science, Umeå University, SE-901 87 Umeå, Sweden (email: {emad, noreland, eddie.wadbro, martin.berggren}@cs.umu.se) and Department of Engineering Sciences, Ångström Laboratory, Uppsala University, Sweden (Robin.Augustine@angstrom.uu.se).

This article has been accepted for publication in a future issue of this journal, but has not been fully edited. Content may change prior to final publication. Citation information: DOI 10.1109/TAP.2015.2449894, IEEE Transactions on Antennas and Propagation

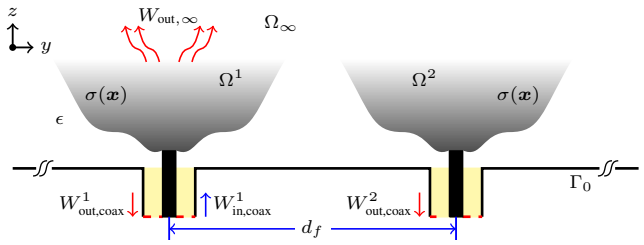

Fig. 1: The design domains Ω^1 and Ω^2 are connected to the inner probes of two 50 Ohm coaxial cables that are separated by a distance d_f.

respectively. Inside Ω^1 and Ω^2, we optimize the conductivity σ such that each antenna radiates efficiently and the coupling coefficient between the two antennas is maximized over a wide frequency band. We require that the two antennas are mirror images of each other and explicitly impose this symmetry in the numerical experiments.

Let Ω_∞ be the analysis domain illustrated in Fig. 1. Inside this domain, the 3D Maxwell equations govern the relation between the electric field $\boldsymbol{E}$ and the magnetic field $\boldsymbol{H}$,

$$\frac{\partial}{\partial t}\mu\boldsymbol{H} + \nabla\times\boldsymbol{E} = \boldsymbol{0}, \tag{1a}$$

$$\frac{\partial}{\partial t}\epsilon\boldsymbol{E} + \sigma\boldsymbol{E} - \nabla\times\boldsymbol{H} = \boldsymbol{0}, \tag{1b}$$

where μ, ϵ, and σ are the permeability, the permittivity, and the conductivity of the medium. Here, we assume that there are no external sources and that the background medium occupying $\Omega_\infty\backslash(\Omega_1\cup\Omega_2)$ is either free-space or a good dielectric. The ground plane Γ_0 and the boundaries of the coaxial cables are the only predefined metallic objects (copper with $\sigma = 5.8\times 10^7$ S/m). Under the assumption that only the TEM mode is supported inside the coaxial cables, the following 1D transport equation is satisfied [9],

$$\frac{\partial}{\partial t}\left(V \pm Z_{\text{c}} I\right) \pm c\frac{\partial}{\partial z}\left(V \pm Z_{\text{c}} I\right) = 0, \tag{2}$$

where V, I, c, and Z_{c} are the potential difference, the current (positive in the z direction), the phase velocity, and the characteristic impedance inside the coaxial cable, respectively. The two terms $V + Z_{\text{c}}I$ and $V - Z_{\text{c}}I$ constitute two signals travelling inside the coaxial cable in the positive and negative z directions, respectively.

Under the assumption that Antenna 1 is transmitting and Antenna 2 is only receiving, we can write an energy balance for the system as

$$W^1_{\text{in,coax}} = W^1_{\text{out,coax}} + W^2_{\text{out,coax}} + W_{\text{out},\infty} + W^1_\Omega + W^2_\Omega, \tag{3}$$

where the left hand side $W^1_{\text{in,coax}}$ indicates an incoming energy, through the first coaxial cable, and the right hand side represents the total outgoing energy, which comprises the reflected energy in the first coaxial cable $W^1_{\text{out,coax}}$, the coupled energy to the second coaxial cable $W^2_{\text{out,coax}}$, the energy radiated to the far-field $W_{\text{out},\infty}$, and the ohmic losses W^1_Ω and W^2_Ω inside Ω^1 and Ω^2, respectively. Note that from energy balance (3), for a given $W^1_{\text{in,coax}}$, maximization of the second term on the right, $W^2_{\text{out,coax}}$, implicitly implies the minimization of the sum of the remaining terms. In order to obtain antennas with better reflection coefficients, we prioritise the minimization of the reflected energy, $W^1_{\text{out,coax}}$, by including that term explicitly in our objective function formulation. Thus, we chose to minimize

$$\log\left(\frac{W^1_{\text{out,coax}}}{W^2_{\text{out,coax}}}\right). \tag{4}$$

IV. Numerical Treatment

We numerically solve the time-domain Maxwell's equations by the FDTD method with a uniaxial perfectly matched layer (UPML) simulating the open space radiation condition [17], [18]. For each Yee edge i in the design domain Ω_1, we want to determine whether associated conductivity σ_i should correspond to free-space or metal to minimize objective function (4). Since the electric field is associated with edges in the Yee grid, the choice of the edge conductivities as design variables gives the most fine-grained description possible of the antenna's conductivity distribution. To avoid solving an intractable non-linear integer programming problem, we allow intermediate conductivities and use a gradient-based optimization algorithm. Here, we compute the gradient of the objective function by the adjoint-field method [9], [19], [20].

The intermediate conductivities give rise to energy losses W^1_Ω and W^2_Ω that can be much larger than $W^2_{\text{out,coax}}$. Thus, to maximize $W^2_{\text{out,coax}}$, a naively implemented gradient-based optimization algorithm will immediately attempt to minimize the energy losses, W^1_Ω and W^2_Ω, and quickly get stuck in a lossless design consisting of only metal or free-space, since any change in the conductivity away from the extreme values will increase the losses. In other words, such an optimization problem is strongly *self-penalizing* towards the lossless case.

To circumvent the self-penalization, we associate with each edge i a design variable $p_i \in [0,1]$ and define the conductivity through $\boldsymbol{\sigma} = 10^{(9\boldsymbol{K}_R\boldsymbol{p}-4)}$, where the exponentiation is taken element-wise and the so-called filtering $\boldsymbol{K}_R\boldsymbol{p}$ corresponds to a weighted local averaging of the variables $\boldsymbol{p}$ over a region with radius R. The filtering effectively blurs the conductivities and thus imposes energy losses inside the design domain. When the filter radius is sufficiently large ($R > \Delta/\sqrt{2}$, where Δ is the size of Yee grid), this strategy ensures that the optimization algorithm cannot get stuck in a lossless case.

To design the antennas, we solve the problem

$$\begin{aligned} \min_{\boldsymbol{p}\in\mathbb{R}^M} \quad & \log\left(\frac{W^1_{\text{out,coax}}(\sigma(\boldsymbol{p}))}{W^2_{\text{out,coax}}(\sigma(\boldsymbol{p}))}\right), \\ \text{s.t.} \quad & 0 \le p_i \le 1 \quad \forall i, \\ & \text{the governing equations.} \end{aligned} \tag{5}$$

To solve problem (5), we solve a sequence of problems with decreasing filter radius R [9]. More precisely, we start with a large filter radius $R_0 = 30\Delta$ and solve optimization problem (5), with initial guess $p_i = 0.7$ for all i, by using the globally convergent method of moving asymptotes (GCMMA) [21] to update the design variables. After partial convergence of sub-problem n, measured in terms of the first order necessary conditions, we reduce the filter radius by setting $R_{n+1} = 0.8R_n$ and solve the design problem on level

This article has been accepted for publication in a future issue of this journal, but has not been fully edited. Content may change prior to final publication. Citation information: DOI 10.1109/TAP.2015.2449894, IEEE Transactions on Antennas and Propagation

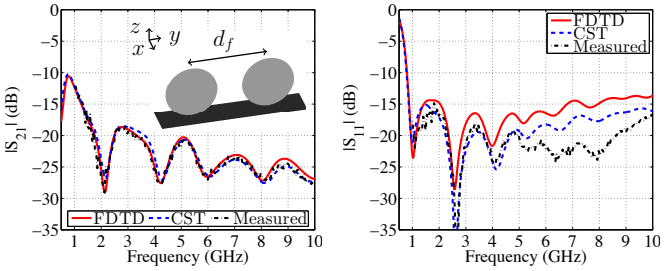

Fig. 2: (a) The coupling coefficient between two 80.5 mm diameter circular disc monopoles separated by a feed-to-feed distance $d_f = 116.90$ mm. (b) The reflection coefficient.

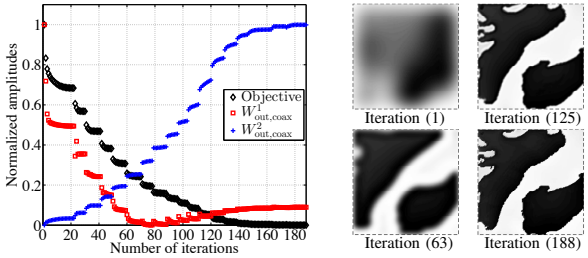

Fig. 3: (a) The progress of the objective function together with the outgoing energies $W^1_{\text{out,coax}}$ and $W^2_{\text{out,coax}}$. (b) The antenna design at some selected iterations, good conductor (black) good dielectric (white).

$n+1$ with the design optimized on level n as initial guess. The procedure ends when the filter radius is so small that we obtain the unfiltered case ($\boldsymbol{\sigma} = 10^{(9\boldsymbol{p}-4)}$).

V. Results and Discussions

A. Antenna design

For the purpose of comparison, we consider as a reference two circular disc monopole antennas, an antenna type that generally shows an ultra-wideband impedance matching with a stable omni-directional radiation pattern [1], [2]. Each monopole consists of a 80.5 mm diameter copper disc located 0.557 mm above the ground plane and connected to a 50 Ohm coaxial cable. The two monopoles have a feed-to-feed separation of $d_f = 116.9$ mm. The performance of the antennas is evaluated by measurements using the Agilent Technologies E8364B vector network analyzer, as well as by simulations with our FDTD code and the CST package. We used 100 μm thick circular discs in the measurements and within the CST package, while in the FDTD simulations, the disc edge is staircased over a planar surface in a uniform Yee grid with size $\Delta = 0.557$ mm. Fig. 2a shows that the coupling between the two disc monopoles has a peak value of -10.6 dB only at the lower frequency limit. Then, the coupling coefficient generally decreases with increasing frequency with some dips occurring close to frequencies for which the antenna size is a multiple of $\lambda/2$ (λ is the free-space wavelength). Fig. 2b shows that the circular disc monopole has a reflection coefficient below -10 dB over the frequency band 0.77–10 GHz.

We solve problem (5) in order to maximize the coupling coefficient and minimize the reflection coefficient over the frequency band 1–10 GHz. This frequency band is imposed by feeding the antenna with a modulated time-domain *sinc* signal. For each monopole, we use a design area of 77.94 mm$\times$77.94 mm located on one side of an FR4 substrate ($\epsilon_r = 4.4$, thickness $= 1.67$ mm, $\tan\delta = 0.001$) and 0.557 mm above the ground plane. The two monopoles are separated by the same feed-to-feed distance as the reference discs ($d_f = 116.90$ mm). Each design domain is discretized by 140×140 Yee cell faces, which yields $39,480$ design variables. To speed up the computations, the implementation of the FDTD method employs graphics processing units (GPU). One FDTD simulation takes around 4 minutes and around 8 GB of memory is required for the gradient computations.

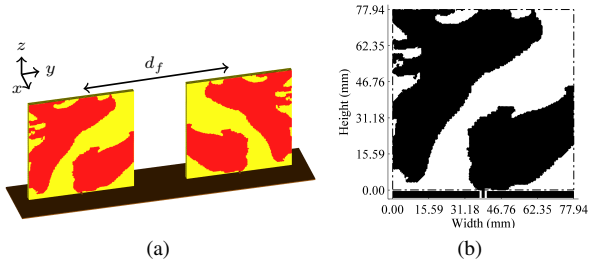

Fig. 4: (a) The geometry of the optimized antennas separated by $d_f = 116.90$ mm. (b) The conductivity distribution over the design space marked by a dash-dot line.

Fig 3a shows the progress of the objective function during the optimization process together with the development of the outgoing energies $W^1_{\text{out,coax}}$ and $W^2_{\text{out,coax}}$. We note the monotonic decrease of the total objective function and that the total number of iterations, 188, is two orders of magnitude smaller than the number of design variables. Note that, in each iteration the FDTD code is called 3–5 times, where 3 calls are used for computing the objective function and its gradient, and 0–2 calls might be used by the GCMMA algorithm to find suitable updates. The sudden jumps in the objective function that occur between consecutive sub-problems where the filter radius decreases, are due to a decrease in the amount of losses inside the design domain. Figure 3b shows the antenna design at some selected iterations. As can be noticed, the gray color (the intermediate values) dominates the antenna design in the beginning, but by the end of optimization process, the antenna consists mainly of either a good conductor (black color) or a good dielectric (white color). Finally, a threshold conductivity $\sigma_{\text{th}} = 0.1$ S/m is used to map conductivities below and above σ_{th} to 0 S/m and 5.8×10^7 S/m, respectively. The final design shown in Fig 4 comprises two parts; an active part connected to the coaxial feed and a passive part that acts as a reflector.

Fig. 5 shows the coupling and the reflection coefficients of the final design evaluated experimentally and through

This article has been accepted for publication in a future issue of this journal, but has not been fully edited. Content may change prior to final publication. Citation information: DOI 10.1109/TAP.2015.2449894, IEEE Transactions on Antennas and Propagation

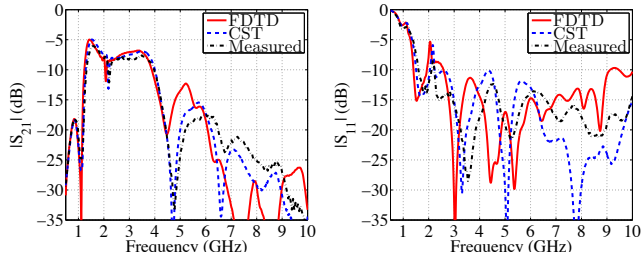

Fig. 5: (a) The coupling coefficient between the two monopoles given in Fig. 4. (b) The reflection coefficient.

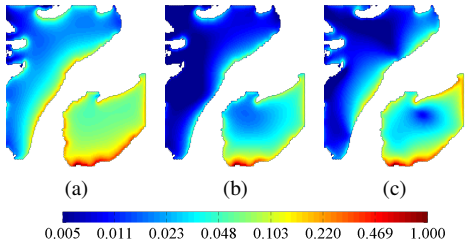

Fig. 6: The normalized surface current over the conductive parts of the optimized antenna given in Fig. 4, computed at (a) 1.5 GHz, (b) 2.5 GHz, and (c) 3.5 GHz.

simulations. The manufacturing of the antennas was carried out by etching of a single sided copper clad FR4 substrate. The differences between simulation and measurements might be caused by differences in geometry description caused by staircase boundaries. The two monopoles have on average a coupling coefficient of -7.5 dB over the frequency band 1.2–3.9 GHz, and the reflection coefficient of each monopole is below -10 dB over the frequency band 1.4–10 GHz. Close to 2 GHz, there is a dip in the $|S_{21}|$ curve and a corresponding peak in the $|S_{11}|$ curve. The reason for this peak could be a resonance effect related to the design domain size, which is approximately $\lambda/2$ around 2 GHz. We noticed for the circular disc monopole that the $|S_{21}|$ curve shows a minimum around 2 GHz, see Fig. 2a. Since the energy of the coupled signal appears in the denominator of the objective function (4), the optimization algorithm is expected to prioritize that term compared to the numerator term W^1_{out} in the beginning of the optimization process (when the coupled energy is very small), which can lead to a trade-off in terms of a peak in the $|S_{11}|$ response. The tendency of the optimization algorithm to prioritize the denominator term $W^2_{\text{out,coax}}$ can be further seen in Fig. 3, where $W^2_{\text{out,coax}}$ is monotonically increasing, while $W^1_{\text{out,coax}}$ is not monotonically decreasing. We discuss some further investigations on this issue in the next section.

Fig. 6 shows the amplitude of the normalized surface current over the conductive parts of the antenna, computed at 1.5, 2.5, and 3.5 GHz. Generally, the current peaks appear over the radiating part connected to the coaxial probe. The current distribution on the reflector part indicates its essential role in the antenna radiation. The surface current spreads over a larger area of the reflector at lower frequencies. As the frequency increases, the peaks of the current are confined closer to the boundaries both on the radiator and the reflector parts.

B. Additional numerical investigations

The two monopoles have electrically shorter separation distance at the lower frequencies, which makes it easier for the optimization algorithm to improve the coupling for these frequencies, as can be seen in Fig. 5a and also in Fig. 2. We tried to improve the performance at higher frequencies by modifying the objective function, for instance by formulating the objective function as weighted linear or non-linear combinations of $W^1_{\text{out,coax}}$ and $W^2_{\text{out,coax}}$. Also, we investigated objective functions that divide the frequency band of interest into smaller bands for which higher frequency terms are prioritized. However, none of the above modifications were successful to improve the performance. We therefore proceeded to explore two modifications of the conceptual setup.

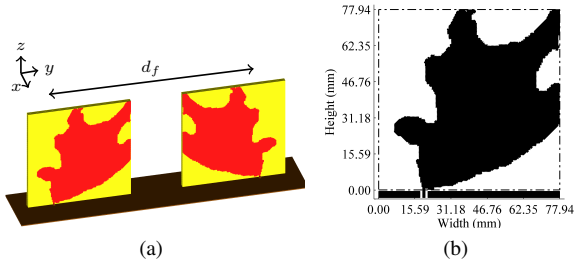

Fig. 7: (a) The geometry of the optimized antennas with $d_f = 155.88$ mm and 38.97 mm edge-to-edge separation. (b) The conductivity over the design space marked by a dash-dot line.

First, we investigated the effect of the feed position. Moving the feed position such that $d_f = 155.88$, but keeping the edge-to-edge separation as the previous case, the optimization algorithm converged in 297 iterations to the design given in Fig. 7. As can be noticed, the obtained design has geometrical similarities to the Vivaldi antenna. However, here the antenna is fed by a coaxial cable, while Vivaldi and antipodal Vivaldi antennas are commonly fed by microstrip-to-slot or microstrip lines, respectively. The lower tapered boundary is similar to the exponential shape of the Vivaldi antennas. However, on the upper boundary appear some protrusions acting like matching stubs. Fig. 8 shows the coupling and reflection coefficients of the antenna. The $|S_{21}|$ curve has an average value of -8.16 dB over the frequency band 0.66–5.0 GHz. We note the dip close to 2 GHz, which was observed for the previous design as well. The $|S_{11}|$ curve is lower than -10 dB over the frequency band 0.75–9.9 GHz, excluding the peak close to 2 GHz. Compared to the previous case, the current design lacks the reflector part, which might explain the reason for the reduced coupling at the lower frequencies. Fig. 9 shows the amplitude of the normalized surface current over the conductive part of the antenna at 1.5, 2.5, 3.5, and 4.5 GHz.

Second, we attempt to improve the performance by optimizing the conductivity over three layers of the FR4 substrate,

This article has been accepted for publication in a future issue of this journal, but has not been fully edited. Content may change prior to final publication. Citation information: DOI 10.1109/TAP.2015.2449894, IEEE Transactions on Antennas and Propagation

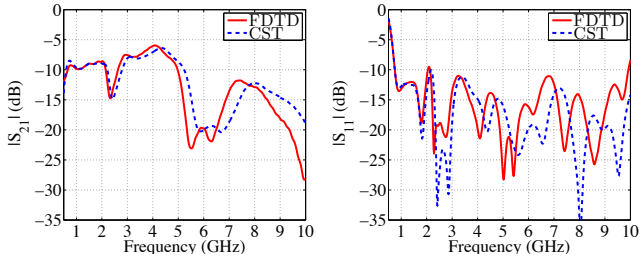

Fig. 8: (a) The coupling coefficient between the two monopoles given in Fig. 7. (b) The reflection coefficient.

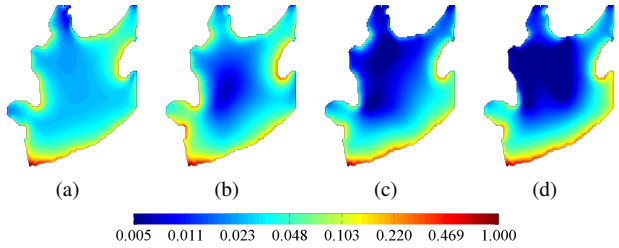

Fig. 9: The normalized surface current over the conductive parts of the optimized antenna given in Fig. 7, computed at (a) 1.5 GHz, (b) 2.5 GHz, (c) 3.5 GHz, and (d) 4.5 GHz.

separated by a distance 15.03 mm, see Fig 10. This design problem has 3 times the number of design variables, that is 118, 440 design variables, compared to the previous cases. Here, we used the same initial settings for the optimization process as in the single layer case with the coaxial feed connected to the center of the middle layer. The design algorithm converged to the final solution, shown in Fig 10, in 204 iterations. (We attach a movie, available online, to show the progress of the design.) The outer layers (Fig. 10b and Fig. 10d) are totally passive and comprise two parts, a reflector part and a director part. The middle layer contains the main radiating element and some small reflecting parts.

Fig 11 shows the coupling and the reflection coefficients of the three-layer optimized antenna. The antenna has an average coupling coefficient of -6.7 dB over the frequency band 0.87–4.87 GHz, which corresponds to a 0.8 dB higher amplitude and a 1.3 GHz wider bandwidth compared to the single-layer monopole case. Further, around 6.5 GHz, the $|S_{21}|$ curve has a peak with value close to -10 dB. The $|S_{11}|$ curve is below -10 dB over the frequency band 1.16–10 GHz, excluding a peak with amplitude -7.7 dB around 2 GHz, which can be interpreted similarly as for the single-layer design cases.

C. Sensitivity to nearby objects

With medical applications in mind, we demonstrate the capabilities of the optimized antennas for detection of nearby objects. As a representative of muscle tissue, a homogeneous phantom material with similar electrical properties is used, see Fig. 12. An $80\times80\times10$ mm^3 slice of the phantom material is

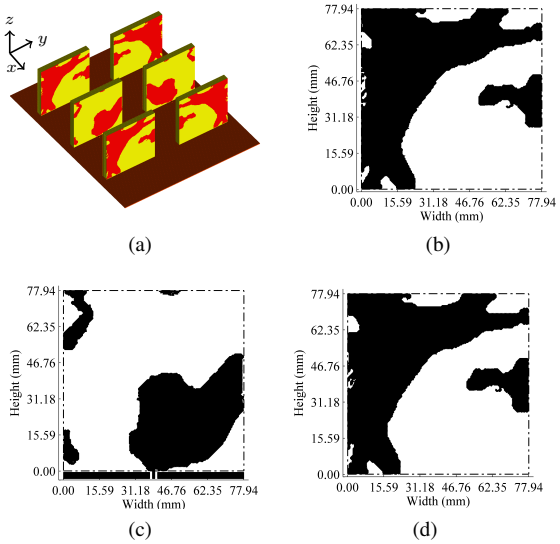

Fig. 10: (a) The geometry of the three-layer optimized antenna with 15.03 mm distance between the layers. (b), (c), and (d) The conductivity distribution starting from the layer closest to the origin and moving toward the positive x-axis, respectively.

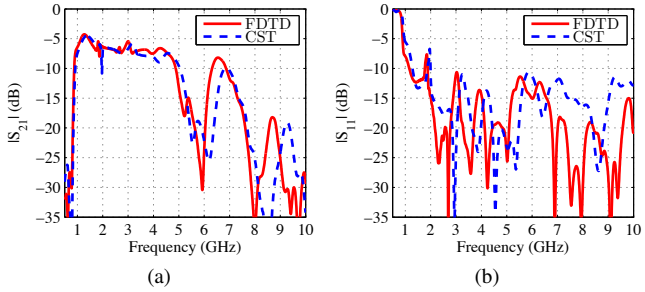

Fig. 11: (a) The coupling coefficient between the three-layer antennas in Fig. 10. (b) The reflection coefficient.

prepared. The slice is positioned between the two antennas, using the same setup as in the antenna optimization, and the scattering parameters of the antennas are used to sense the phantom. Fig. 13 shows the arrangement of the antennas and the phantom. The phantom is highly compliant and in order to support the slice, supporting frames of a light foam material were added. No effect on the scattering parameters was observed from insertion alone of the supporting frames between the antennas. We study the detection sensitivity, measured as the difference in the scattering parameters between the cases presence and absence of the phantom, that is, we compute $(|S_{ij}^{\text{Phantom}} - S_{ij}^{\text{Air}}|)$ for $i, j = 1, 2$.

The differences in the S_{11} and S_{21} parameters of the antenna pairs are shown in Fig. 14 with the slice placed symmetrically between the antennas. We note that the change in the coupling coefficient (S_{21}) is very accurately predicted by the model, and that the detection sensitivity is roughly four times larger and covering a wider frequency band for the optimized antennas compared to the disc monopoles. Also the detection sensitivity

This article has been accepted for publication in a future issue of this journal, but has not been fully edited. Content may change prior to final publication. Citation information: DOI 10.1109/TAP.2015.2449894, IEEE Transactions on Antennas and Propagation

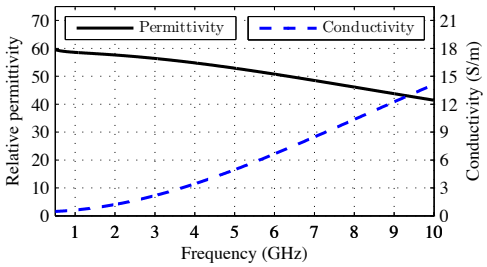

Fig. 12: The phantom electrical properties versus frequency.

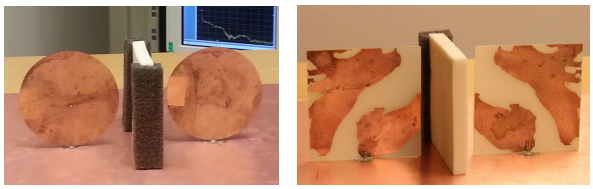

Fig. 13: Setup with a muscle tissue phantom slab placed between two antennas.

for the reflection coefficient S_{11} is increased considerably, but the fit between the model and the measurements is somewhat worse.

VI. Conclusion

The problem of designing planar wideband directive antennas is formulated as a computationally efficient optimization problem. The fact that each edge inside the design domain grid is subject to design allowed the algorithm not only to optimize the active radiating part but also to build passive parts (reflectors or directors) that contribute to the improvement of the overall performance. The experimental and simulation results showed that the optimized antennas could be good candidates to increase the sensitivity of microwave detection and imaging systems. Optimizing antennas in a background medium other than the free-space or for pure far-field directivity could be subjects of future work.

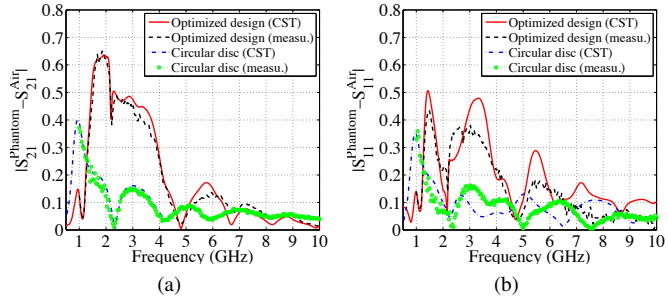

Fig. 14: (a) The difference between the coupling coefficients in presence and absence of $80\times80\times10$ mm^3 phantom, for the optimized antenna and the disc monopole. (b) The difference in the reflection coefficients.

Acknowledgment

The computations were performed on resources provided by the Swedish National Infrastructure for Computing (SNIC) at the center for scientific and technical computing (Lunarc) and at the High Performance Computing Center North (HPC2N). This research was supported in part by the Swedish Foundation for Strategic Research Grant No. AM13-0029, and the Swedish Research Council No. 621-2013-3706. The authors thank Professor A. Rydberg, Department of Engineering Sciences, Uppsala University, for valuable feedback.

References

[1] S. Honda, "A disk monopole antenna with 1:8 impedance bandwidth and omnidirectional radiation pattern," in *IEEE AP-S Int. Symp.*, 1992.

[2] H. Jafari, M. Deen, S. Hranilovic, and N. Nikolova, "A study of ultrawideband antennas for near-field imaging," *IEEE Trans. Antennas Propag.*, vol. 55, no. 4, pp. 1184–1188, Apr. 2007.

[3] C. A. Balanis, *Antenna Theory: Analysis and Design*, 3rd ed. Wiley-Interscience, 2005.

[4] P. Gibson, "The Vivaldi aerial," in *Microwave Conference, 1979. 9th European*, Sep. 1979, pp. 101–105.

[5] J. Langley, P. Hall, and P. Newham, "Novel ultrawide-bandwidth Vivaldi antenna with low crosspolarisation," *Electronics Letters*, vol. 29, no. 23, pp. 2004–2005, Nov. 1993.

[6] J. Bourqui, M. Okoniewski, and E. Fear, "Balanced antipodal Vivaldi antenna with dielectric director for near-field microwave imaging," *IEEE Trans. Antennas Propag.*, vol. 58, no. 7, pp. 2318–2326, Jul. 2010.

[7] M. Gustafsson and D. Sjöberg, "Physical bounds and sum rules for high-impedance surfaces," *IEEE Trans. Antennas Propag.*, vol. 59, no. 6, pp. 2196–2204, Jun. 2011.

[8] J. Yang and A. Kishk, "A novel low-profile compact directional ultra-wideband antenna: The self-grounded bow-tie antenna," *IEEE Trans. Antennas Propag.*, vol. 60, no. 3, pp. 1214–1220, Mar. 2012.

[9] E. Hassan, E. Wadbro, and M. Berggren, "Topology optimization of metallic antennas," *IEEE Trans. Antennas Propag.*, vol. 62, no. 5, pp. 2488–2500, May 2014.

[10] ——, "Patch and ground plane design of microstrip antennas by material distribution topology optimization," *Progress In Electromagnetics Research B*, vol. 59, pp. 89–102, 2014.

[11] M. P. Bendsøe and O. Sigmund, *Topology Optimization. Theory, Methods, and Applications*. Springer, 2003.

[12] A. Diaz and O. Sigmund, "A topology optimization method for design of negative permeability metamaterials," *Struct. Multidiscip. Optim.*, vol. 41, pp. 163–177, 2010.

[13] A. Erentok and O. Sigmund, "Topology optimization of sub-wavelength antennas," *IEEE Trans. Antennas Propag.*, vol. 59, no. 1, pp. 58 –69, Jan. 2011.

[14] N. Aage, "Topology optimization of radio frequency and microwave structures," Ph.D. dissertation, Technical University of Denmark, 2011.

[15] T. Nomura, M. Ohkado, P. Schmalenberg, J. Lee, O. Ahmed, and M. Bakr, "Topology optimization method for microstrips using boundary condition representation and adjoint analysis," in *European Microwave Conference (EuMC2013)*, Oct 2013, pp. 632–635.

[16] S. Zhou, W. Li, and Q. Li, "Level-set based topology optimization for electromagnetic dipole antenna design," *J. Comput. Phys.*, vol. 229, no. 19, pp. 6915 – 6930, 2010.

[17] K. Yee, "Numerical solution of initial boundary value problems involving Maxwell's equations in isotropic media," *IEEE Trans. Antennas Propag.*, vol. 14, no. 3, pp. 302 –307, May 1966.

[18] A. Taflove and S. Hagness, *Computational Electrodynamics: The Finite-Difference Time-Domain Method*, 3rd ed. Artech House, 2005.

[19] Y.-S. Chung, C. Cheon, I.-H. Park, and S.-Y. Hahn, "Optimal design method for microwave device using time domain method and design sensitivity analysis. II. FDTD case," *IEEE Trans. Magn.*, vol. 37, no. 5, pp. 3255 –3259, Sep. 2001.

[20] N. Nikolova, H. Tam, and M. Bakr, "Sensitivity analysis with the FDTD method on structured grids," *IEEE Trans. Microw. Theory Tech.*, vol. 52, no. 4, pp. 1207 – 1216, Apr. 2004.

[21] K. Svanberg, "A class of globally convergent optimization methods based on conservative convex separable approximations," *SIAM J. Optim.*, vol. 12, no. 2, pp. 555–573, 2002.